applied sciences

MDPI

Article

Corrosion Protection Evaluation of Mild Steel: The Role of Hybrid Materials Loaded with Inhibitors

Ioannis A. Kartsonakis and Costas A. Charitidis *

Research Unit of Advanced, Composite, Nano-Materials and Nanotechnology, School of Chemical Engineering, National Technical University of Athens, GR-15773 Athens, Greece; ikartso@chemeng.ntua.gr

* Correspondence: charitidis@chemeng.ntua.gr; Tel.: +30-210-772-4046

Received: 4 August 2020; Accepted: 18 September 2020; Published: 21 September 2020

Featured Application: The $Ce_xTi_yO_z$ nanocontainers that fabricated and loaded with 5-amino-1, 3,4-thiadiazole-2-thiol in this work, can be used in the interior side of mild steel pipelines conveying liquids in order to protect them from corrosion.

Abstract: In the present work, an assessment of the corrosion behavior of mild steel in the presence of an organic corrosion inhibitor loaded into hybrid composite materials is performed. Hybrid organic–inorganic nanocontainers based on cerium and titanium oxides were fabricated via a combination of radical polymerization together with the coprecipitation method and sol-gel technique. The corrosion inhibition role of these hybrid materials loaded with an inhibitor is considered. A set of characterization assays addressing morphology, composition and structural aspects of the exposed steels is illustrated, along with electrochemical evaluations. The results reveal enhanced stimuli responsive anticorrosion ability of the produced hybrid materials. Furthermore, upon corrosion, new compounds are formed onto the exposed areas of the treated metals. The conducted experiments shed light on the corrosion mechanisms for steel alloys as well as the actuation of the fabricated composite materials, paving the way for future developments in this area.

Keywords: steel; EIS (electrochemical impedance spectroscopy); Raman spectroscopy; hybrid materials

1. Introduction

During the recent years, steel has become one of the most widely used alloys in the sectors of railways and road constructions, as well as in buildings and infrastructures. Steel skeletons are employed for the fabrication of several structures such as bridges, skyscrapers, stadiums and airports [1]. In addition, iron alloys are commonly used in medical, military and aerospace applications because they exhibit enhanced mechanical and tensile strength together with their improved conductivity and ductility properties [2]. Among iron alloys, carbon steel is employed as a construction material for pipeline transport production and processing related industries [2–4]. The reason is that carbon steel exhibits enhanced mechanical strength and low cost. Steel is assumed to be carbon steel when carbon is the major constituent apart from iron and the carbon content is below wt.% 2.40 [5]. Based on the amount of carbon, three major types of carbon steel exist: low (mild) carbon steel (wt.% 0.04–0.30), medium carbon steel (wt.% 0.31–0.60) and high carbon steel (wt.% 0.61–2.40). The increase in carbon percentage results in an increase in hardness and a decrease in ductility [6]. The difference between carbon steel and black steel is that black steel is fabricated from nongalvanized steel, whereas carbon steel needs galvanization because of its susceptibility to corrosion. Black steel is important in applications where there is no need for galvanized steel. Black steel pipes are seamless, uncoated and

widely used for transporting either gas or water for commercial or residential buildings because these pipes are better fire retardants than galvanized pipes and due to the high strength of the steel [4].

Despite the fact that the aforementioned forms of steel have several applications, these types of steel exhibit poor performance in aggressive corrosive environments [7,8]; their exposure to these types of environments give rise to corrosion processes [9]. Therefore, the identification and development of new groups of protective compounds able to attenuate this problem are required. Several methods have been employed for the metal corrosion protection such as application of coatings [4,10,11] and the use of corrosion inhibitors [8,12,13]; one of the most widespread methods against corrosion is the use of organic compounds. Organic inhibitors are very efficient for mild steel, due to the fact that they contain atoms such as sulfur, oxygen and nitrogen that result in the enhanced adsorption onto a metal surface [14]. Furthermore, the presence of aromatic and aliphatic functional groups with double and triple bonds also plays a crucial role in their improved metal surface adsorption [15]. Thus, the organic molecule adsorption onto the steel surface results in the isolation of the metal alloy from the aggressive environment improving the metal corrosion resistance.

The motivation for this work is the assessment of the corrosion behavior of mild steel in the presence of potential corrosion inhibitor 5-amino-1,3,4-thiadiazole-2-thiol (ATT) loaded into hybrid material. Taking into account our previous studies based on mild steel [16] together with the additional experiments that were conducted on the protection of mild steel related to the corrosion protection effectiveness of potential inhibitor ATT loaded in cerium-titanium oxide ($Ce_xTi_yO_z$) nanocontainers, the main aim of this study is to present the role of corrosion inhibitors either in free form or loaded into containers and their potential effect to the corrosion protection mechanisms of steel.

In the literature, studies have been conducted on the evaluation of ATT as a corrosion inhibitor on several metal alloys. According to the work of Yang et al. [17], the interaction of ATT with silver panels results in the formation of ATT monolayers onto the silver surface. The type of monolayer depends on the pH of the electrolytic solution. The group of Sethuramanet al. [18] investigated the corrosion inhibition of copper in 3.5% NaCl medium by the formation of a film based on ATT and TiO_2 that was applied onto the copper surface via electrodeposition. The obtained results revealed that the fabricated film has an enhanced inhibitive effect on the copper corrosion protection. Furthermore, the inhibition effect of ATT on the corrosion of mild steel in 1 M HCl solution was studied by the group of Bentiss et al. [19]. They found that ATT acts as a good inhibitor in this acid medium, with the formation of an inhibitive layer consisting of an iron oxide/hydroxide mixture where 5-ATT molecules are encapsulated. In addition, the corrosion protection of mild steel using ATT was also studied by the group of Solmaz et al. [20]. They found that ATT demonstrated inhibition efficiency for the corrosion of mild steel in acidic solution (0.5M HCl) due to the formation of a film that was adsorbed on the surface of the mild steel. Finally, in our previous studies [21], it was proved that ATT can be considered as a corrosion inhibitor for hot dip galvanized steel by due to the formation of a film between the zinc and the nitrogen or sulfur atoms of the organic compound.

The main goal of the presented study is to discern if ATT that contains both sulfur and nitrogen atoms performs as an inhibitor in the aforementioned corrosion process restriction. In this regard, the effect of organic compound is reported, after exposing steel specimens to corrosive environments in its presence. The obtained results are discussed taking into account our previous studies based on the corrosion protection of mild steel [16]. The importance of these experiments is precisely combined with the current urgent requirement for corrosion protection of steel pipelines. On this subject, the protection effectiveness of the complexes, oxides or salts that are created on either mild steel surface, as well as the morphological conversions that occur on the surface of the metal alloy panels following exposure in the presence or absence of inhibitors, are reported based on three families of techniques: electrochemical, microscopy and spectroscopy.

The originality and novelty of the present research rests upon the type of corrosion inhibitor studied loaded into hybrid materials and on the corrosion behavior of mild steel in NaCl electrolyte. The inhibitor ATT contains three nitrogen and two sulfur atoms that can act as electron donors; there is a

possibility that it is enhanced due to the existence of resonance of the molecule structure. The obtained results are analyzed and discussed in accordance with our previous studies based on the evaluation of several compounds as potential corrosion inhibitors for mild steel. Finally, it may be highlighted that the added value of our work resides in the correlation of the steel corrosion mechanisms with the presence of hybrid materials that utilized as carriers, fabricated though combination of multiple processes and techniques such as sol-gel process, radical polymerization and the coprecipitation method.

2. Materials and Methods

2.1. Materials

The experiments were conducted using analytical reagent grade chemicals. Potassium persulfate (KPS, Sigma-Aldrich, St. Louis, MO, USA), polyvinylpyrrolidone (PVP, average molecular weight: 55,000, Sigma-Aldrich, St. Louis, MO, USA), 5-amino-1,3,4-thiadiazole-2-thiol (ATT, Acros-Organics, Geel, Belgium), cerium nitrate ($Ce(NO_3)_3$, Sigma Aldrich, St. Louis, MO, USA), titanium tetraisopropoxide (TTIP, Sigma Aldrich, St. Louis, MO, USA), acetone (Sigma-Aldrich, St. Louis, MO, USA), sodium dodecyl sulphate (SDS, Sigma-Aldrich, St. Louis, MO, USA), absolute ethanol (Sigma Aldrich, St. Louis, MO, USA), sodium chloride (Sigma Aldrich, St. Louis, MO, USA) and sodium hydroxide (Sigma Aldrich, St. Louis, MO, USA), were used as received. The monomer methacrylic acid (MAA, Sigma-Aldrich, St. Louis, MO, USA) was double distilled under reduced pressure prior to use. Hot-rolled (non-galvanized) mild steel panels were received from TMK-ARTROM S.A., together with all the required certifications (ASTM A568/A568M-09). Electrochemical measurements were performed on a mild steel grade API 5L X42 conveying pipeline with its chemical composition presented in Table 1.

Table 1. Chemical composition of mild steel grade API 5L X42 conveying pipeline.

Composition	C	Mn	S	P	Si	Ni	Cr	Mo	Cu	Al	N	V + Ti + Nb	Fe
(wt.%)	0.15	0.56	0.002	0.12	0.21	0.07	0.04	0.01	0.22	0.02	0.009	0.004	as remainder

2.2. Preparation of Substrates

The cleaning procedure for the mild steel substrates was accomplished according to ASTM D6386-99 (reapproved 2005). At first, they were abraded with SiC paper up to 5 μm grain size (P4000), and then they were immersed in a mixture of ethanol and acetone (50:50) of purity 96% *v/v* for 20 min. After that, they were subjected to a NaOH solution of pH 11 for 5 min at 60 °C. Finally, the substrates were rinsed with distilled water and dried in a desiccator. This process is necessary because of the formation of a variety of iron oxides such as α-FeO(OH), β-FeO(OH), γ-FeO(OH) and Fe_3O_4 onto the metal surface after their exposure to the environment [22]. All substrates were abraded again with SiC paper up to 5 μm grain size (P4000) prior to their use in the electrochemical characterizations. All the aforementioned cleaning procedures are necessary in order to perform the removal of oils, grease and caked-on dirt; the removal of scale and oxide films by pickling.

2.3. Synthesis and Loading of Nanocontainers

Hollow nanocontainers of $Ce_xTi_yO_z$ were fabricated with a combination of the synthetic procedures demonstrated in our previous studies [23,24]. A three-step procedure was followed. At first, cores of polymethacrylic (PMAA) were produced via radical polymerization. These cores were used as templates and coated with cerium-titanium oxide inorganic shell using $Ce(NO_3)_3$ and TTIP as precursors via the coprecipitation method and sol gel process. Then, the templates were removed through rinsing with ethanol resulting in the production of $Ce_xTi_yO_z$ hollow spheres (nanocontainers). These materials were synthesized in order to be used as carriers for ATT corrosion inhibitors. The loading of the nanocontainers was accomplished according to our previous work [25]. For this reason, the empty nanocontainers were placed into a chamber, vacuum was applied and then saturated solution of ATT in acetone was injected into the chamber. The mixture of ATT solution with nanocontainers was left

under stirring overnight, and then the loaded nanocontainers were collected after centrifugation of the mixture.

2.4. Characterization

The microscale information related to the morphology of the substrates was collected with Scanning Electron Microscopy (SEM) imaging performance using a Hitachi Tabletop Microscope TM3030 equipped with an energy dispersive X-ray spectrophotometer (EDS) system (QUANTAX 70). Transmission electron microscopy (TEM) was used for the morphology, size and composition estimation of the produced nanocontainers using a Jeol 2100 HR (200 kV, resolution 0.23 nm). The loading of the nanocontainers with ATT was assessed with thermal degradation of the loaded materials via thermogravimetric analysis (TGA) and differential scanning calorimetry using a thermal analyzer apparatus (STA 449 F5 Jupiter). The samples were measured under constant nitrogen flow (50 mL/min) plus nitrogen flow as a protective gas (20 mL/min) from 25 to 1000 °C at a heating rate of 10 °C/min. The instrument was calibrated both for temperature and sensitivity prior to the nonisothermal experiments. Proteus 6.1 Software was used for the manipulation of the exported data. The structure of the produced materials was studied via XRD measurements. The crystal structure was identified by powder X-ray diffraction using X Bruker D8 Advance Twin Twin, employing Cu-Kα radiation (λ = 1.5418 Å). Micro-Raman spectroscopy was used for the chemical analysis via a Renishaw in Via spectrometer working in backscattering configuration and equipped with a near-infrared diode laser emitting at 532 nm. For the spectra recording, the laser beam was focused on the sample surface and the light power was adjusted to provide 1 mW for a 1 μm diameter spot.

The effectiveness assessment of the ATT corrosion inhibitor due to its release from $Ce_xTi_yO_z$ nanocontainers as well as the verification of the corresponding corrosion mechanisms were evaluated using electrochemical impedance spectroscopy (EIS). For this purpose, mixtures of loaded nanocontainers in a corrosive environment of NaCl 3.5 wt.% solutions were used. The solutions of NaCl 3.5 wt.% were prepared with distilled water. The loaded nanocontainers were added into the electrolytic solution (NaCl 3.5 wt.%) [25]. As the immersion time of the mild steel into the electrolytic solution (corrosive environment) elapses, the inhibitor is released from the nanocontainers and is adsorbed onto the steel surface. Taking into account the TGA results denoting that the $Ce_xTi_yO_z$ nanocontainers are ~32 wt.% loaded with ATT (as it is discussed in detail in Section 3.1.2) as well as the low solubility of ATT corrosion inhibitor in water (0.5 mg/100 g), the content of loaded nanocontainers in NaCl solution was 0.050 w/v in order for saturated solutions of ATT to be obtained.

The EIS measurements were performed utilizing a galvanostat/potentiostat in connection with a frequency response analyzer (VersaStat 3/FRA, PAR AMETEK) together with an electrochemical cell of three electrodes (K0235 Flat Cell Kit, AMETEK), consisting of a platinum mesh electrode as the counting electrode, a saturated silver/silver chloride electrode (Ag/AgCl, KCl (sat)) as a reference electrode and a working electrode (~1 cm^2 exposed geometric area of the sample surface). The applied sinusoidal perturbation was 10 mV in a measurement frequency range from 100 kHz to 0.01 Hz. The obtained spectra were interpreted through ZView® software (Scribner Associates) using the appropriate equivalent electrochemical circuit each time. All the electrochemical characterizations were conducted in a pH range from 6.92 to 7.74. The samples were in vertical position, and three repetition measurements were taken at room temperature for every result.

The EIS results were interpreted by numerical fitting using equivalent electric circuit models. Due to the electrode heterogeneity, constant phase elements (CPE) were used. According to the literature, the CPE is related to a distribution of the capacitance over a surface or its changes with frequency which are associated with electrode heterogeneity [26]. When the phase shift of a capacitor is different from −90°, a modification has to be assumed by using CPE instead of pure capacitors in the equivalent circuits [26]. The impedance of an R-CPE parallel association is given by (Equation (1)):

$$Z_{R-CPE} = \frac{R}{1 + RY_0(j\omega)^n} \quad (1)$$

where Y_0 is the admittance of the CPE and n is the CPE exponent. The n takes the values: 1 when it corresponds to a capacitor; $0.5 < n < 1$ when a nonideal capacitor behavior takes place; 0.5 when the CPE describes a diffusion process and represents a Warburg impedance; and finally, 0 when it represents a resistor [27]. Using the Cole–Cole approach together with CPE [28,29], the capacitance can be calculated by numerical fitting through the Equation (2):

$$C = \sqrt[n]{\frac{RY_0}{R^n}} \quad (2)$$

Equation (3) was applied for the corrosion inhibition efficiency, $\eta(\%)$, assessment:

$$\eta(\%) = \frac{R_{ct(inhibitor)} - R_{ct(bareMetal)}}{R_{ct(inhibitor)}} \times 100, \quad (3)$$

where $R_{ct(inhibitor)}$ and $R_{ct(bareMetal)}$ are assigned to the charge transfer resistances in the presence and in the absence of an inhibitor, respectively.

3. Results and Discussion

3.1. Characterization of Nanocontainers

3.1.1. Transmission Electron Microscopy and Energy Dispersive X-ray Spectroscopy

The morphology of the nanocontainers is illustrated in Figure 1. Taking into account the TEM images, it is observed that they are hollow spheres with a diameter of 180 ± 40 nm. The presence of the ATT compound loaded into the nanocontainers is also depicted. From the corresponding EDS analysis, it is clearly denoted that the fabricated nanocontainers consisted of cerium, titanium and oxygen elements (Table 2). The existence of sulfur and carbon is assigned to the ATT.

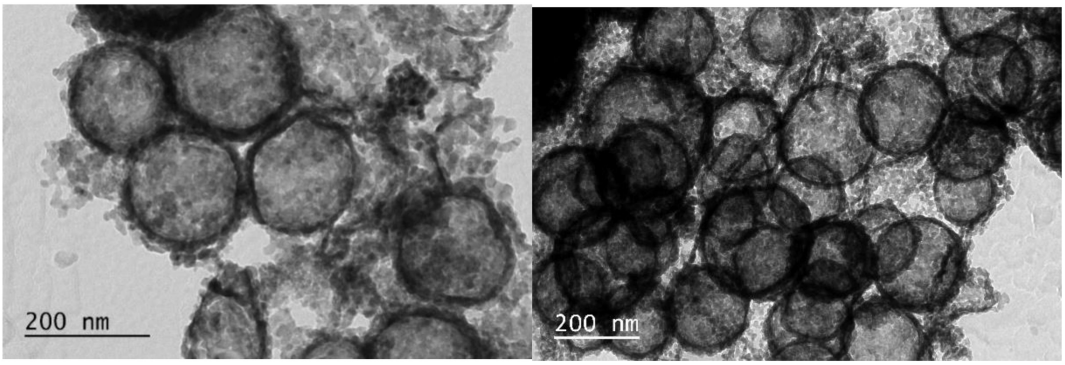

Figure 1. TEM images of $Ce_xTi_yO_z$ nanocontainers loaded with ATT.

Table 2. Tabulated values of the EDS analysis of the $Ce_xTi_yO_z$ nanocontainers loaded with ATT.

Element	C	O	Na	Si	S	K	Ti	Ce
(wt.%)	24.11	2.93	0.24	0.48	4.16	0.28	60.17	7.63

3.1.2. Thermogravimetric Analysis and Differential Scanning Calorimetry

The TGA-DSC diagrams of $Ce_xTi_yO_z$ nanocontainers loaded with ATT are depicted in Figure 2. Regarding the TGA diagram, it may be remarked that there was a weight loss of ~8% from 50 to 180 °C that is assigned to the desorption of acetone, ethanol and physically adsorbed water (free and physisorbed water) [30]. The second weight loss ~10% between 180 and 260 °C is ascribed to oxidative degradation of the ATT that is on the nanocontainers' shell. The third sharp weight loss ~22% from 260 to 520 °C is attributed to the oxidative degradation of the ATT that was inside the nanocontainers.

The broad exothermic peak from 260 to 520 °C in the DSC diagram corresponds to the oxidative degradation of the ATT. Taking into account the aforementioned results, it should be mentioned that the $Ce_xTi_yO_z$ nanocontainers were ~32 wt.% loaded with ATT.

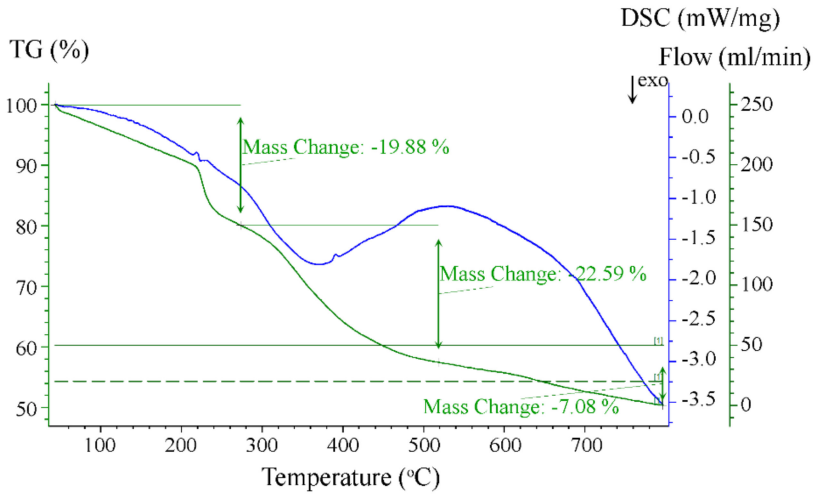

Figure 2. TGA and DSC diagrams of $Ce_xTi_yO_z$ nanocontainers loaded with ATT.

3.1.3. Fourier Transform Infra-Red Spectroscopy

Figure 3 illustrates the FT-IR spectra for the $Ce_xTi_yO_z$ nanocontainers loaded with ATT. The wavenumber region between 400 and 1000 cm^{-1} included bands indicative of metal oxygen bonding. The absorption peaks of TiO_2 were at 496, 567, 674 and 760 cm^{-1} [31,32]. In the region between 425 and 540 cm^{-1} the CeO_2 characteristic peaks appeared [23]. The broad bands in the range of 3100–3324 cm^{-1} are assigned to the stretching vibration of O–H bond of the physically adsorbed water in the sample [32]. The characteristic peaks of ATT also appeared. The peaks at 1557 and at 2910 cm^{-1} are ascribed to the N-H deformation/bending vibrations as well as stretching vibrations, respectively. The C=N stretching vibration appeared in the peaks 1460, 1605 and 2100 cm^{-1}. The presence of C-N was confirmed by the peaks at 1060 and 1306 cm^{-1} [33]. The peaks at 787 and 1005 cm^{-1} are due to the C-S stretching vibrations. The existence of C=S stretching vibrations can be proved by the peaks at 1145 and 1236 cm^{-1} [34].

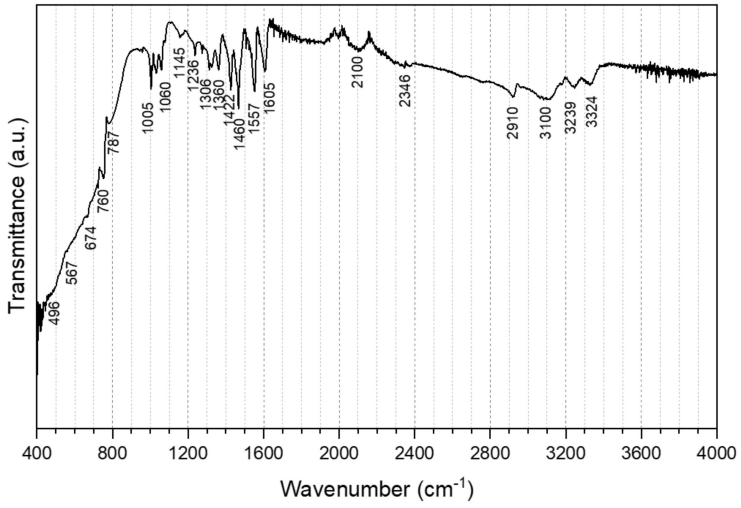

Figure 3. FT-IR spectrum of $Ce_xTi_yO_z$ nanocontainers loaded with ATT.

3.1.4. X-ray Diffraction Analysis

The XRD pattern in Figure 4 demonstrates the titanium oxide, cerium oxide and cerium titanium oxide phases that were formatted and consisted of the nanocontainer's shell. Taking into account that the peaks are very narrow, it can be assumed that the nanocontainers are crystalline. The position of the peaks indicate that they consist of the types: TiO_2 anatase (89-4921, syn), $Ti_{0.936}O_2$ rutile (89-0554, syn), cerium (38-0765), $Ce_{11}O_{20}$ cerium oxide (89-8435), CeO_{2-x} cerium oxide (49-1415) and Ce_2TiO_5 cerium titanium oxide (49-1606). Considering the aforementioned types, it may be remarked that the produced nanocontainers consist of cerium titanium oxide phases together with cerium oxide and titanium oxide. This result can be assigned to the different reactivity of the inorganic precursors of TTIP and $Ce(NO_3)_3$ during their hydrolysis and condensation reactions.

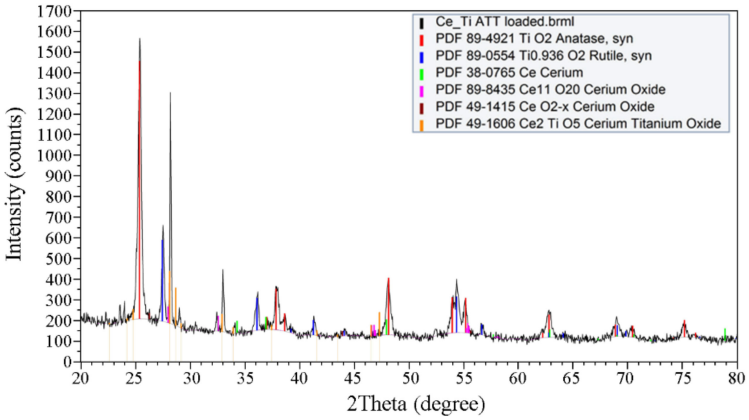

Figure 4. XRD pattern of $Ce_xTi_yO_z$ nanocontainers loaded with ATT.

3.2. Corrosion Protection Evaluation

3.2.1. Scanning Electron Microscopy and Energy Dispersive X-ray Spectroscopy

The SEM images of the mild steel panel prior its subjection to corrosive environment (Mild Steel-blank) are depicted in Figure 5. Taking into account these images, the existence of scratches and dents on the metal surface that are ascribed to either the fabrication of the specimens or the cleaning process can be observed. Considering the EDS analysis, it can be seen that the wt.% iron concentration was 95.1, whereas the oxygen concentration was roughly 1.7, denoting the absence of iron oxide products (Table 3).

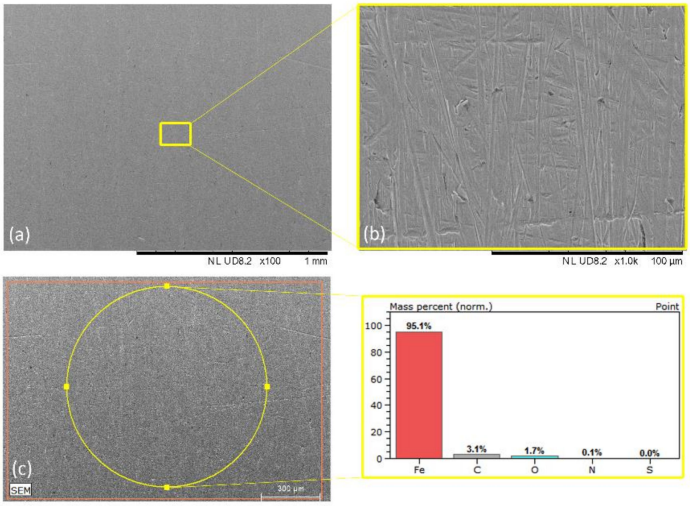

Figure 5. (**a**,**b**) SEM images and the corresponding (**c**) EDS analysis of mild steel (Mild Steel-blank).

The SEM images as well as the corresponding EDS analysis of the mild steel panel surface after its exposure to 3.5 wt.% NaCl for 144 h in the absence of inhibitors (Mild Steel-3.5%NaCl) are illustrated in Figure 6. Considering these images, it is clearly denoted that the mild steel surface has been damaged due to the presence of the corrosive environment. Signs of etched layers appear onto the metal surface that can be attributed to the corrosion phenomena accelerated by chloride anions.

Crystalline tubular forms appear that are assigned to either hematite or goethite or lepidocrocite [35–37]. The corresponding EDS analysis depicts elevated oxygen value concentration compare to that of the sample Mild Steel-blank due to the formation of the previously mentioned iron oxides (Table 3).

Table 3. Tabulated values of wt.% element concentration of mild steel panels prior and after their exposure to 3.5 wt.% NaCl, for 144 h, in the presence of $Ce_xTi_yO_z$ nanocontainers loaded with ATT or not.

Sample	Spectrum at	wt.% Element Concentration				
		O	Fe	C	S	N
Mild Steel-blank	Figure 5	1.7	96.1	3.1	-	-
Mild Steel-3.5%NaCl	Figure 6	47.7	46.8	5.5	-	-
Mild Steel-3.5%NaCl-ATT	Figure 7d	12.2	11.6	18.4	30.8	27.0
Mild Steel-3.5%NaCl-ATT	Figure 7e	9.8	20.2	11.9	43.9	14.2
Mild Steel-3.5%NaCl-ATT	Figure 7f	32.5	50.6	6.5	5.9	4.6
Mild Steel-3.5%NaCl-ATT	Figure 7g	30.6	29.7	8.9	20.4	10.5
Mild Steel-3.5%NaCl-ATT	Figure 7h	33.3	42.6	8.5	7.9	7.6
Mild Steel-3.5%NaCl-ATT	Figure 7i	11.0	11.1	18.0	32.8	27.0

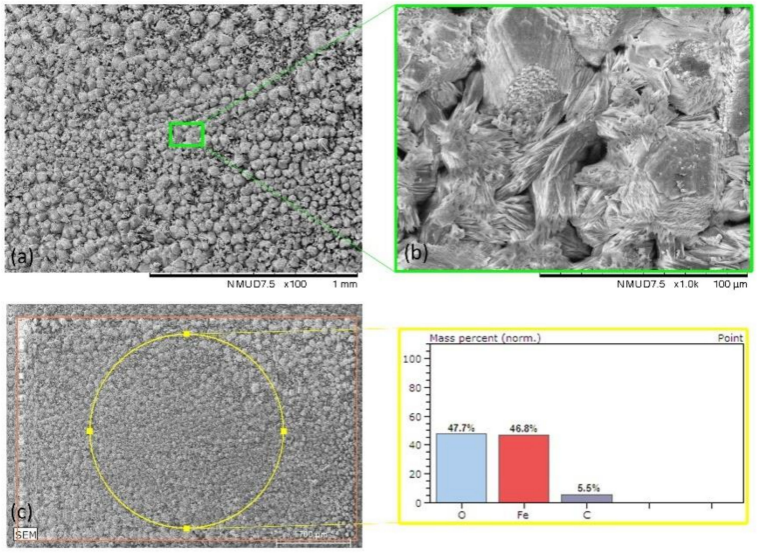

Figure 6. (**a**,**b**) SEM images and the corresponding (**c**) EDS analysis of mild steel immersed into 3.5 wt.% NaCl for 144 h (Mild Steel-3.5%NaCl).

The surface SEM images of Mild Steel-3.5%NaCl-ATT after subjection to 3.5 wt.% NaCl for 144 h are illustrated in Figure 7. It can be seen that layers of spongy agglomerations were created (Figure 7a). According to the literature, these agglomerations can be assigned to maghemite, lepidocrocite and precursors of green rust (as magnetite), created in the saline solution [38] because of the prolonged exposure process [37,39]. Furthermore, several lamellas structures are observed [37] that can be ascribed to hematite and goethite α phases [40–42] (Figure 7c). The ruptured layer indicates the inhibitor (ATT) interaction with the metal surface [41,43,44] (Figure 7b). The corresponding EDS analysis of Figure 7d–i reveals elevated oxygen wt.% concentration compare to that of the sample Mild Steel-blank because of the aforementioned iron oxides formation along with the presence of sulfur and nitrogen that are ascribed to the adsorbed organic ATT (Table 3).

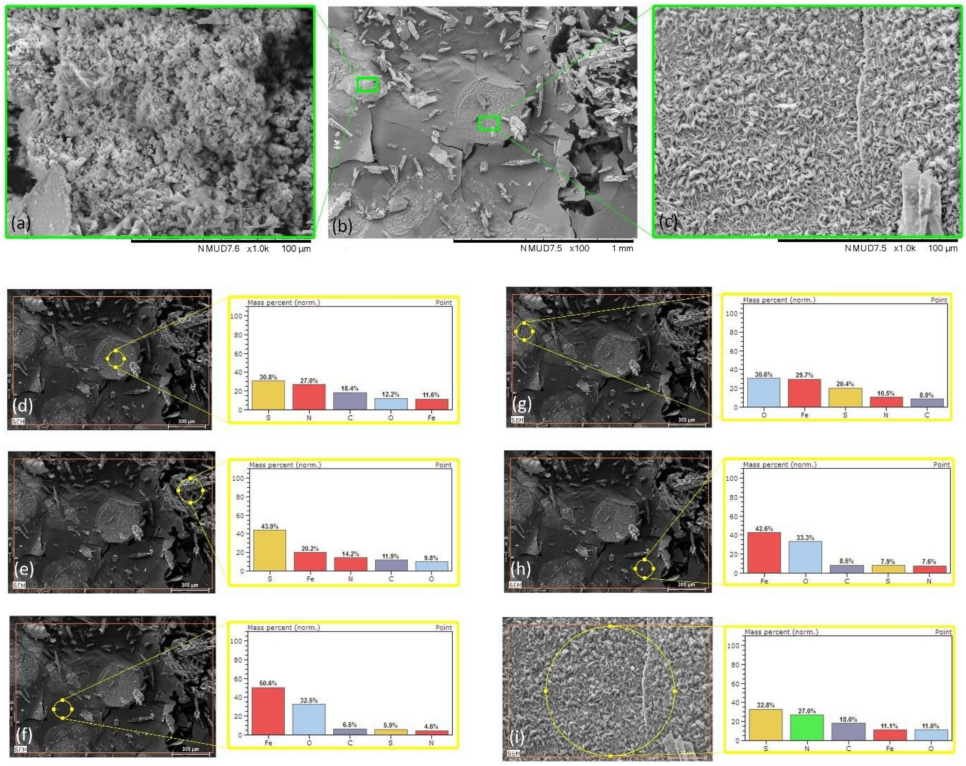

Figure 7. (**a**–**c**) SEM images and the corresponding (**d**–**i**) EDS analyzes of mild steel immersed into 3.5 wt.% NaCl for 144 h in the presence of $Ce_xTi_yO_z$ nanocontainers loaded with ATT (Mild Steel-3.5%NaCl-ATT).

3.2.2. RAMAN Spectroscopy

The adsorption of ATT onto mild steel was also evaluated by Raman spectroscopy. Figure 8 illustrates the corresponding spectra of mild steel panels after exposure to a corrosive environment for 144 h, in the presence or absence of $Ce_xTi_yO_z$ nanocontainers loaded with ATT. The identification of the corresponding Raman spectra peaks is tabulated in Table 4. Considering the Mild Steel-3.5%NaCl, (Figure 8a) the characteristic peaks of iron oxides due to corrosion process can be clearly observed. The compounds hematite (α-Fe_2O_3) [45], lepidocrocide (γ-FeOOH) [46], goethite (β-FeOOH) [47], magnetite (Fe_3O_4) [48], feroxyhyte (δ-FeOOH) [45], are clearly seen in the region 154–393 cm^{-1}. The presence of maghemite(γ-Fe_2O_3) is confirmed by the peaks at 715 and 776 cm^{-1} [48]. The peak at 683 cm^{-1} is assigned to goethite [45,49], whereas the peaks at 1362 and 1613 cm^{-1} are attributed to ferrihydrite ($Fe_5HO_8{\cdot}4H_2O$) [45,50]. Finally, the peak at 154 cm^{-1} is ascribed to the symmetric stretch of interlayer chloride ions in iron oxide (green rust) [51].

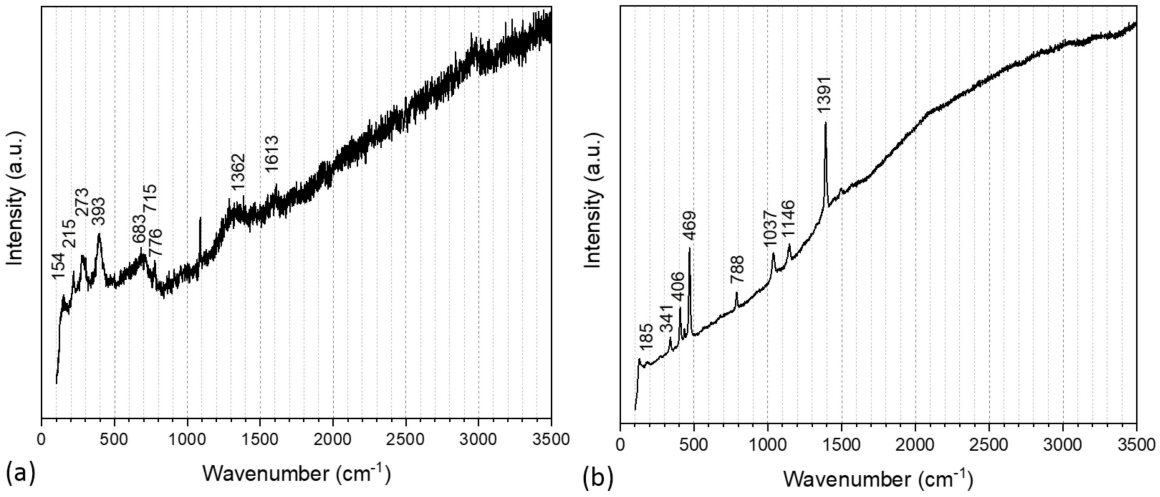

Figure 8. Raman spectra of mild steel immersed into 3.5 wt.% NaCl for 144 h: (**a**) Mild Steel-3.5%NaCl, (**b**) Mild Steel-3.5%NaCl-ATT.

Table 4. Classification of the Raman spectra peaks.

Main Raman Peaks (cm^{-1})	Assignment	Samples
154	symmetric stretch of interlayer chloride ions in green rust	Mild Steel-3.5%NaCl
215	hematite	
273	goethite	
393	lepidocrocide	
683	magnetite	
715	maghemite	
776	maghemite	
1362	ferrihydrite	
1613	ferrihydrite	
185	symmetric stretch of interlayer chloride ions in green rust	Mild Steel-3.5%NaCl-ATT
341	Fe-S due to ATT	
406	NCS of the ring due to ATT	
469	Fe-S due to ATT	
788	N-H out of plane due to ATT	
1037	N-N due to ATT	
1146	C-N due to ATT	
1391	C-N due to ATT	

Regarding the Mild Steel-3.5%NaCl-ATT, several peaks confirm the adsorption of ATT onto the mild steel surface (Figure 8b). The peaks at 341 and 469 cm^{-1} are considered to be caused by the Fe-S bond vibration created by the chemisorption of ATT [52,53]. The peak at 406 cm^{-1} is attributed to the NCS of the ring vibration due to ATT [54]. The peak at 788 cm^{-1} is assigned to the N-H out of plane stretching due to ATT [55]. Furthermore, the N-N vibration due to ATT appears at the peak 1037 cm^{-1}. In addition, the peaks at 1146 and 1391 cm^{-1} are ascribed to the C-N vibration due to ATT [54]. Finally, the peak at 185 cm^{-1} is attributed to the symmetric stretch of interlayer chloride ions in iron oxide (green rust) [51].

3.2.3. Electrochemical Studies

The EIS plots of mild steel panels in the presence or absence of $Ce_xTi_yO_z$ nanocontainers loaded with ATT after exposure to the corrosive environment are depicted in Figure 9. Considering the EIS Bode curves after 24 h of immersion, it is clearly denoted that the presence of the inhibitor resulted in a

higher EIS modulus compared to that of the Mild Steel-3.5%NaCl indicating an increase in the mild steel corrosion protection. The same results were obtained after 144 h of exposure to 3.5 wt.%NaCl indicating improved corrosion protection of mild steel due to the introduction of $Ce_xTi_yO_z$ nanocontainers loaded with ATT inhibitor and the consequent release of the inhibitor.

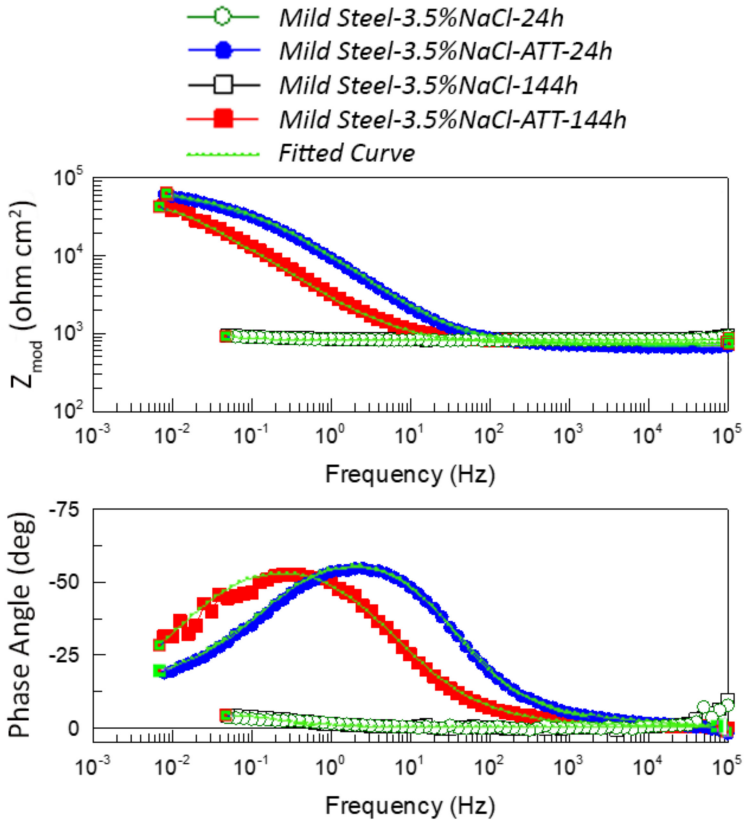

Figure 9. EIS plots recorded after exposure to 3.5 wt.% NaCl for: 24 h Mild Steel-3.5NaCl, (open circle); 24 h Mild Steel-3.5NaCl-ATT, (filled circle); 144 h Mild Steel-3.5NaCl, (open square); 144 h Mild Steel-3.5NaCl-ATT, (filled square).

The EIS Bode plots for both the untreated mild steel after exposure to 3.5 wt.% NaCl (Mild Steel-3.5NaCl) for either 24 or 144 h can be described with one time constant in the low frequency range that is attributed to the corrosion process. On the other hand, the systems including $Ce_xTi_yO_z$ nanocontainers loaded with ATT inhibitor (Mild Steel-3.5NaCl-ATT) after exposure to 3.5 wt.% NaCl for either 24 or 144 h can be characterized with one in the middle frequency range that is ascribed to a film formation between the mild steel surface and the ATT compounds, and a second one in the middle–low frequency range that is assigned to the corrosion process. However, as the immersion time elapsed from 24 to 144 h, the relative time constant moved to lower frequencies because of the increase in the corrosion active area and the corresponding double layer capacitance enhancement.

The equivalent circuit for both the untreated mild steels after exposure to 3.5 wt.% NaCl (Mild Steel-3.5NaCl) for either 24 or 144 included three components and corresponded to an EIS spectrum comprising of one time constant. In particular, it consisted of the solution resistance (R_{sol}), the charge transfer resistance together with a double layer CPE (R_{ct}-CPE_{dl}) that are attributed to the presence of corrosion active pits at the mild steel surface Figure 10A.

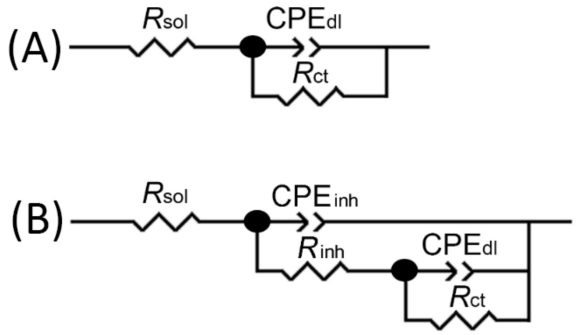

Figure 10. Equivalent circuits used for numerical simulation of the EIS data: (**A**) equivalent circuit with 3 elements, (**B**) equivalent circuit with 5 elements.

Considering the systems including $Ce_xTi_yO_z$ nanocontainers loaded with ATT inhibitor (Mild Steel-3.5NaCl-ATT) after exposure to 3.5 wt.% NaCl for either 24 or 144 h, the relative equivalent circuit consisted of five components and corresponded to an EIS spectra of two relaxation times (Figure 10B). More specifically, it included the resistance of the solution (R_{sol}), the pore resistance and the CPE of the inhibitor layer (R_{inh}-CPE_{inh}) in parallel connection that are attributed to the response of the electrolyte inside the pores of the layer, and finally, the charge transfer resistance and the double layer CPE (R_{ct}-CPE_{dl}) that are due to the presence of corrosion process.

Taking into account the aforementioned Equation (2), the C_{inh} and C_{dl} parameters were determined (Table 5). In principle, the C_{dl} value is influenced by the roughness of metal surface [8,12]. However, considering the CPE_{inh}-P value (CPE_{inh}-P represents the n, which is the CPE exponent in Equations (1) and (2)) calculated for the sample Mild Steel-3.5%NaCl-ATT (00.48632) after subjection in corrosive environment for 24 h, it may be remarked that this element cannot be associated to a nonideal capacitor [26]. Nonetheless, it should be pointed that a Warburg impedance component introduction did not improve the numerical fitting of the EIS results.

Table 5. Fitting parameters according to equivalent circuits of Figure 10 obtained for the mild steel subjected in corrosive environment.

24 h into 3.5 wt.%NaCl	**Mild Steel-3.5%NaCl**	**Mild Steel-3.5%NaCl-ATT**
CPE_{inh}-T ($\mu F\ cm^{-2}\ s^{-n}$)	-	26.333
CPE_{inh}-P	-	0.73644
R_{inh}(kohm cm^2)	-	46.019
C_{inh} ($mF\ cm^{-2}$)	-	0.33420
CPE_{dl}-T ($mF\ cm^{-2}\ s^{-n}$)	12.358	0.13117
CPE_{dl}-P	0.78496	0.48632
R_{ct}(kohm cm^2)	0.184	82.241
C_{dl} ($mF\ cm^{-2}$)	15.476	1.6175
η%	-	99.77
144 h into 3.5 wt.%NaCl	**Mild Steel-3.5%NaCl**	**Mild Steel-3.5%NaCl-ATT**
CPE_{inh}-T ($\mu F\ cm^{-2}\ s^{-n}$)	-	94.663
CPE_{inh}-P	-	0.71006
R_{inh}(kohm cm^2)	-	52.700
C_{inh} ($mF\ cm^{-2}$)	-	3.0632
CPE_{dl}-T ($mF\ cm^{-2}\ s^{-n}$)	10.619	0.73004
CPE_{dl}-P	0.74194	0.99998
R_{ct}(kohm cm^2)	0.154	14.845
C_{dl} ($mF\ cm^{-2}$)	12.600	0.73007
η%	-	98.96

Analyzing the determined values of Table 5, it is important to notice that the introduction of $Ce_xTi_yO_z$ nanocontainers loaded with ATT into the electrolytic solution results in an enhancement of R_{ct} values for both the exposure time intervals. It is highlighted that high R_{ct} values denote enhanced resistance to the corrosion process [56]. On the contrary, the lower C_{dl} values that were obtained in the presence of $Ce_xTi_yO_z$ nanocontainers loaded with ATT into the corrosive environment revealed a low corrosion reaction area [56]. The reduction in the area is assigned to the water molecule replacement by the corrosion inhibitor molecules due to their adsorption on the metal surface resulting in the increase in the electrical double layer thickness [57]. In sum, according to the aforementioned results, it can be assumed that the inhibitor ATT provides effective corrosion protection to mild steel. This outcome is also confirmed by the enhanced values of *η(%)* derived from Equation (3) after 24 and 144 h (99.77% and 98.96%) of mild steel panel exposure to 3.5 wt.% NaCl solution, in the presence or absence of $Ce_xTi_yO_z$ nanocontainers loaded with ATT.

3.2.4. Corrosion Inhibition Mechanism

Taking into consideration the aforementioned results together with our previous studies on mild steel corrosion protection [16], the following corrosion inhibition mechanism can be assumed. Briefly, considering the corrosion mechanism of iron, the exposure of mild steel into saline corrosive environment results in the release of ferrous ions (Fe^{2+}) and ferric ions (Fe^{3+}) ions due to iron oxidation (anodic part), as depicted in reactions 4 and 5. It should be mentioned that in the pH range from 6.92 to 7.74 where the measurements were conducted, there was a reduction in the dissolved O_2 to OH^- ions (reaction 6) that acted as the cathodic part. The produced OH^- reacted with the Fe^{2+}or Fe^{3+}, and iron hydroxides were synthesized (reactions 7, 8) and precipitated onto the corroded metal surface creating a thick gel that is characteristic of wet rapid corrosion [58].

$$Fe \rightarrow Fe^{2+} + 2e^-, \text{anode} \quad (4)$$

$$Fe \rightarrow Fe^{3+} + 3e^-, \text{anode} \quad (5)$$

$$O_2 + 2H_2O + 4e^- \rightarrow 4OH^-, \text{cathode} \quad (6)$$

$$Fe^{+2} + 2OH^- \rightarrow Fe(OH)_2(s), \quad (7)$$

$$Fe^{+3} + 3OH^- \rightarrow Fe(OH)_3(s), \quad (8)$$

In aqueous $NaCl_{(aq)}$ solution, the presence of Cl^- also reacts with the iron cations according to the reactions 9 and 10 forming intermediate compounds. Then, these compounds react with water producing highly soluble iron hydroxide compounds and HCl (reactions 11, 12) [1]. Furthermore, the reaction between iron oxides and hydroxides causes the production of another thick gel, [Fe-O-OH], that can further react with iron cations giving additional types of iron oxides that mainly consist of magnetite (Fe_3O_4) (reaction 13).

$$Fe^{+2} + 2Cl^- \rightarrow FeCl_2, \quad (9)$$

$$Fe^{+3} + 3Cl^- \rightarrow FeCl_3, \quad (10)$$

$$FeCl_2 + 2H_2O \rightarrow Fe(OH)_2(s) + 2HCl, \quad (11)$$

$$FeCl_3 + 3H_2O \rightarrow Fe(OH)_3(s) + 3HCl, \quad (12)$$

$$8FeOOH + Fe^{2+} + 2e^- \rightarrow 3Fe_3O_4 + 4H_2O, \quad (13)$$

The formatted magnetite passive film can be deteriorated by the attack of the Cl^- provoking several corrosion phenomena [59].

The corrosion protection effectiveness of ATT can be attributed to its chemisorption onto the mild steel surface, decreasing the dissolution rate of the metal because of an adherent passive film formation [60]. As it was discussed in our previous work [16], the ATT corrosion inhibitor has

an enhanced binding capability to be attached onto the metal surface due to the presence of both nitrogen and sulfur atoms. The reason is that both these elements can act as electron donors [43,61]. This tendency is further increased by the presence of heterocyclic rings on the inhibitor molecule [61,62] and the corresponding resonance existence [63]. According to the work of Ortega-Luoni et al. [64], the ATT can be represented by the tautomers of Figure 11; whereas the thion form predominantly exists. The thion form of ATT can form a stable layer onto the steel surface due to chemical adsorption [65].

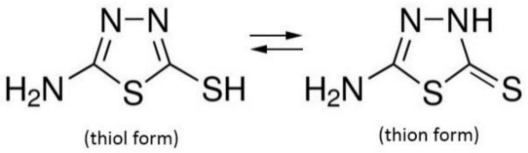

Figure 11. Schematic representation of the thiol and thion forms of ATT.

Figure 12 illustrates the schematic representation of the chemical adsorption of the thion form of ATT onto the surface of the mild steel. It can be seen that a layer of iron oxides was formed onto the steel surface due to its interaction with the environment. The ATT molecules chemically bonded onto this layer.

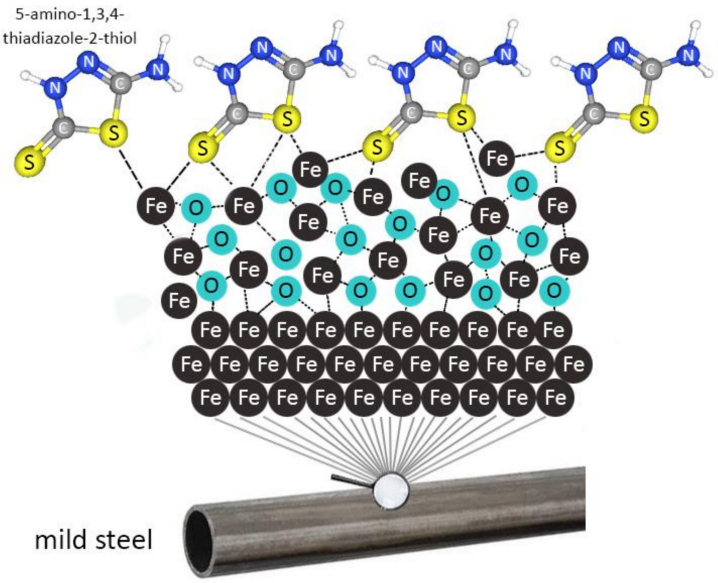

Figure 12. Schematic representation of the ATT connections onto the mild steel surface resulting in the formation of the protective film.

Taking into account the obtained results that were supported with the aforementioned mechanism along with our previous studies on the corrosion behavior of mild steel [16], it may be remarked that the chemical compounds including sulfur and nitrogen atoms can be considered as corrosion inhibitors. The reason is that their ability to exist in tautomer forms enables them to provide electrons to the anodic sides of the corrosion area resulting in their adsorption onto the metal surface creating a layer that insulates the metal from the aggressive ion penetration [15].

4. Conclusions

In the present study, carriers made of hybrid materials were fabricated based on an organic core that was used as template for the production of $Ce_xTi_yO_z$ shells. The successful fabrication of the hybrid material was confirmed by characterizations based on morphology, structure and composition. The produced hollow $Ce_xTi_yO_z$ nanocontainers were loaded with the organic inhibitor ATT and

evaluated for their corrosion inhibition effectiveness onto mild steel using saline water as corrosive environment. According to the obtained results, it can be assumed that the inhibitor ATT provides effective corrosion protection to mild steel. It is mentioned that the calculated values of *η(%)* derived after 24 and 144 h of mild steel panel exposure to 3.5 wt.% NaCl solution, in the presence or absence of $Ce_xTi_yO_z$ nanocontainers loaded with ATT were 99.77% and 98.96%, respectively.

Taking into account that ATT includes polar groups sulfur and nitrogen, there is an increase in the electron density at the reaction center resulting in the formation of chemical bonds between the ATT and the metal. Thus, ATT is adsorbed on the surface of mild steel creating monolayers of ATT compounds on the surface of mild steel due to the lone pair of electrons of the N and S atoms, isolating the metal from aggressive ions. Estimating the morphology, spectroscopy and electrochemical characterizations, the steel corrosion protection mechanisms can be assigned to the formation of protective layers onto the metal surface because of the inhibitor presence that prevents the penetration of chlorides. Furthermore, it was observed that the fabricated $Ce_xTi_yO_z$ nanocontainers can be utilized as carriers of the ATT corrosion inhibitor. Therefore, the system $Ce_xTi_yO_z$ nanocontainers loaded with ATT can be used as potential additives into the industrial conveying API 5L X42 pipeline steels in order to provide a corrosion protection up to 144 h. Our future studies will include the investigation of the aforementioned corrosion inhibitor release from either the $Ce_xTi_yO_z$ nanocontainers or other cerium based nanocontainers for extended periods of exposure to corrosive environments up to 3 months.

Author Contributions: I.A.K. and C.A.C. conceived and designed the experiments. I.A.K. conducted the experiments. I.A.K. performed the characterization and evaluation of the data. I.A.K. and C.A.C. discussed the data and wrote the paper. All authors have read and agreed to the published version of the manuscript.

Funding: This research received no external funding.

Acknowledgments: The authors would like to thank Afroditi Ntziouni for the XRD analysis.

Conflicts of Interest: The authors declare no conflict of interest.

References

1. Verma, C.; Ebenso, E.E.; Quraishi, M.A. Corrosion inhibitors for ferrous and non-ferrous metals and alloys in ionic sodium chloride solutions: A review. *J. Mol. Liq.* **2017**, *248*, 927–942. [CrossRef]
2. Rouzmeh, S.S.; Naderi, R.; Mahdavian, M. A sulfuric acid surface treatment of mild steel for enhancing the protective properties of an organosilane coating. *Prog. Org. Coat.* **2017**, *103*, 156–164. [CrossRef]
3. Khodair, Z.T.; Khadom, A.A.; Jasim, H.A. Corrosion protection of mild steel in different aqueous media via epoxy/nanomaterial coating: Preparation, characterization and mathematical views. *J. Mater. Res. Technol.* **2019**, *8*, 424–435. [CrossRef]
4. Morozov, Y.; Calado, L.M.; Shakoor, R.A.; Raj, R.; Kahraman, R.; Taryba, M.G.; Montemor, M.F. Epoxy coatings modified with a new cerium phosphate inhibitor for smart corrosion protection of steel. *Corros. Sci.* **2019**, *159*, 108128. [CrossRef]
5. Asami, K.; Waseda, Y.; Suzuki, S. (Eds.) Characterization of Rust Layers on a Plain-Carbon Steel and Weathering Steels Exposed to Industrial and Coastal Atmosphere for Years. In *Characterization of Corrosion Products on Steel Surfaces*, 1st ed.; Springer-Verlag: Berlin/Heidelberg, Germany, 2006; pp. 159–197. [CrossRef]
6. Ovid'ko, I.A.; Valiev, R.Z.; Zhu, Y.T. Review on superior strength and enhanced ductility of metallic nanomaterials. *Prog. Mater. Sci.* **2018**, *94*, 462–540. [CrossRef]
7. Prabakaran, M.; Kim, S.-H.; Mugila, N.; Hemapriya, V.; Parameswari, K.; Chitra, S.; Chung, I.-M. Aster koraiensis as nontoxic corrosion inhibitor for mild steel in sulfuric acid. *J. Ind. Eng. Chem.* **2017**, *52*, 235–242. [CrossRef]
8. Fernandes, C.M.; Ferreira Fagundes, T.D.S.; Escarpini dos Santos, N.; de Shewry, M.; Rocha, T.; Garrett, R.; Borges, R.M.; Muricy, G.; Valverde, A.L.; Ponzio, E.A. Ircinia strobilina crude extract as corrosion inhibitor for mild steel in acid medium. *Electrochim. Acta* **2019**, *312*, 137–148. [CrossRef]
9. Gong, W.; Yin, X.; Liu, Y.; Chen, Y.; Yang, W. 2-Amino-4-(4-methoxyphenyl)-thiazole as a novel corrosion inhibitor for mild steel in acidic medium. *Prog. Org. Coat.* **2019**, *126*, 150–161. [CrossRef]

10. Xu, D.; Lou, C.; Huang, J.; Lu, X.; Xin, Z.; Zhou, C. Effect of inhibitor-loaded halloysite nanotubes on active corrosion protection of polybenzoxazine coatings on mild steel. *Prog. Org. Coat.* **2019**, *134*, 126–133. [CrossRef]
11. Alibakhshi, E.; Akbarian, M.; Ramezanzadeh, M.; Ramezanzadeh, B.; Mahdavian, M. Evaluation of the corrosion protection performance of mild steel coated with hybrid sol-gel silane coating in 3.5 wt.% NaCl solution. *Prog. Org. Coat.* **2018**, *123*, 190–200. [CrossRef]
12. Luo, X.; Ci, C.; Li, J.; Lin, K.; Du, S.; Zhang, H.; Li, X.; Cheng, Y.F.; Zang, J.; Liu, Y. 4-aminoazobenzene modified natural glucomannan as a green eco-friendly inhibitor for the mild steel in 0.5 M HCl solution. *Corros. Sci.* **2019**, *151*, 132–142. [CrossRef]
13. Gholamhosseinzadeh, M.R.; Aghaie, H.; Zandi, M.S.; Giahi, M. Rosuvastatin drug as a green and effective inhibitor for corrosion of mild steel in HCl and H2SO4 solutions. *J. Mater. Res. Technol.* **2019**, *8*, 5314–5324. [CrossRef]
14. Habeeb, H.J.; Luaibi, H.M.; Abdullah, T.A.; Dakhil, R.M.; Kadhum, A.A.H.; Al-Amiery, A.A. Case study on thermal impact of novel corrosion inhibitor on mild steel. *Case Stud. Therm. Eng.* **2018**, *12*, 64–68. [CrossRef]
15. Tsoeunyane, M.G.; Makhatha, M.E.; Arotiba, O.A. Corrosion Inhibition of Mild Steel by Poly(butylene succinate)-L-histidine Extended with 1,6-diisocynatohexane Polymer Composite in 1 M HCl. *Int. J. Corros.* **2019**, *2019*, 1–12. [CrossRef]
16. Kartsonakis, I.A.; Stamatogianni, P.; Karaxi, E.K.; Charitidis, C.A. Comparative Study on the Corrosion Inhibitive Effect of 2-Mecraptobenzothiazole and Na2HPO4 on Industrial Conveying API 5L X42 Pipeline Steel. *Appl. Sci.* **2019**, *10*, 290. [CrossRef]
17. Yang, H.; Song, W.; Ji, J.; Zhu, X.; Sun, Y.; Yang, R.; Zhang, Z. pH-dependent 2-amino-5-mercapto-1,3,4-thiadiazole monolayers at the silver surface: Surface enhanced Raman scattering spectroscopic and electrochemical observations. *Appl. Surf. Sci.* **2008**, *255*, 2994–2999. [CrossRef]
18. Vinothkumar, K.; Sethuraman, M.G. Corrosion inhibition ability of electropolymerised composite film of 2-amino-5-mercapto-1,3,4-thiadiazole/TiO_2 deposited over the copper electrode in neutral medium. *Mater. Today Commun.* **2018**, *14*, 27–39. [CrossRef]
19. Ouici, H.; Tourabi, M.; Benali, O.; Selles, C.; Jama, C.; Zarrouk, A.; Bentiss, F. Adsorption and corrosion inhibition properties of 5-amino 1,3,4-thiadiazole-2-thiol on the mild steel in hydrochloric acid medium: Thermodynamic, surface and electrochemical studies. *J. Electroanal. Chem.* **2017**, *803*, 125–134. [CrossRef]
20. Solmaz, R.; Kardaş, G.; Yazıcı, B.; Erbil, M. Adsorption and corrosion inhibitive properties of 2-amino-5-mercapto-1,3,4-thiadiazole on mild steel in hydrochloric acid media. *Colloids Surf. A Physicochem. Eng. Asp.* **2008**, *312*, 7–17. [CrossRef]
21. Kartsonakis, I.A.; Stanciu, S.G.; Matei, A.A.; Hristu, R.; Karantonis, A.; Charitidis, C.A. A comparative study of corrosion inhibitors on hot-dip galvanized steel. *Corros. Sci.* **2016**, *112*, 289–307. [CrossRef]
22. Matsushima, I. Carbon Steel—Atmospheric Corrosion. In *R. Winston Revie, E.U.s., Corrosion Handbook*; John Wiley & Sons, Inc.: Hoboken, NJ, USA, 2008; pp. 515–528.
23. Mekeridis, E.D.; Kartsonakis, I.A.; Pappas, G.S.; Kordas, G.C. Release studies of corrosion inhibitors from cerium titanium oxide nanocontainers. *J. Nanopart. Res.* **2010**, *13*, 541–554. [CrossRef]
24. Karaxi, E.K.; Kartsonakis, I.A.; Charitidis, C.A. Assessment of Self-Healing Epoxy-Based Coatings Containing Microcapsules Applied on Hot Dipped Galvanized Steel. *Front. Mater.* **2019**, 6. [CrossRef]
25. Kartsonakis, I.A.; Danilidis, I.L.; Pappas, G.S.; Kordas, G.C. Encapsulation and release of corrosion inhibitors into titania nanocontainers. *J. Nanosci. Nanotechnol.* **2010**, *10*, 5912–5920. [CrossRef]
26. Hsu, C.H.; Mansfeld, F. Technical Note:Concerning the Conversion of the Constant Phase Element Parameter Y0into a Capacitance. *Corrosion* **2001**, *57*, 747–748. [CrossRef]
27. Kong, G.; Lingyan, L.; Lu, J.; Che, C.; Zhong, Z. Corrosion behavior of lanthanum-based conversion coating modified with citric acid on hot dip galvanized steel in aerated 1M NaCl solution. *Corros. Sci.* **2011**, *53*, 1621–1626. [CrossRef]
28. Shifler, D.A.; Aylor, D.M. Testing in environments-seawater. In *Corrosion Tests and Standards Application and Interpretation*; Baboian, R., Ed.; ASTM International: Baltimore, MD, USA, 2005; pp. 362–379.
29. Cole, K.S.; Cole, R.H. Dispersion and Absorption in Dielectrics II. Direct Current Characteristics. *J. Chem. Phys.* **1942**, *10*, 98–105. [CrossRef]
30. Takeuchi, M.; Martra, G.; Coluccia, S.; Anpo, M. Investigations of the structure of H2O clusters adsorbed on TiO2 surfaces by near-infrared absorption spectroscopy. *J. Phys. Chem. B* **2005**, *109*, 7387–7391. [CrossRef]

31. Kartsonakis, I.A.; Liatsi, P.; Danilidis, I.; Bouzarelou, D.; Kordas, G. Synthesis, characterization and antibacterial action of hollow titania spheres. *J. Phys. Chem. Solids* **2008**, *69*, 214–221. [CrossRef]
32. Nakamoto, K. (Ed.) *Infrared and Raman Spectra of Inorganic and Coordination Compounds Part B: Applications in Coordination, Organometallic, and Bioinorganic Chemistry*, 6th ed.; John Wiley & Sons, Inc.: Hoboken, NJ, USA, 2009.
33. Socrates, G. (Ed.) Amines, Imines, and Their Hydrohalides. In *Infrared and Raman Characteristic Group Frequencies, Tables and Charts*, 2nd ed.; John Wiley & Sons Ltd.: Baffins Lane, Chichester, West Sussex, UK, 2001; pp. 107–114.
34. Socrates, G. (Ed.) Sulfur and Selinium compounds. In *Infrared and Raman Characteristic Group Frequencies, Tables and Charts*, 2nd ed.; John Wiley & Sons Ltd: Baffins Lane, Chichester, West Sussex, UK, 2001; pp. 209–228.
35. Dwivedi, D.; Lepková, K.; Becker, T. Carbon steel corrosion: A review of key surface properties and characterization methods. *RSC Adv.* **2017**, *7*, 4580–4610. [CrossRef]
36. Cornell, R.M.; Schwertmann, U. *The Iron Oxides: Structure, Properties, Reactions, Occurrences and Uses*, 2nd ed.; Wiley-VCH Verlag GmbH & Co.; KGaA: Weinheim, Germany, 2003.
37. Raman, A.; Nasrazadani, S.; Sharma, L. Morphology of rust phases formed on weathering steels in various laboratory corrosion tests. *Metallography* **1989**, *22*, 79–96. [CrossRef]
38. Refait, P.; Génin, J.M.R. The transformation of chloride-containing green rust one into sulphated green rust two by oxidation in mixed Cl^- and SO_4^{2-} aqueous media. *Corros. Sci.* **1994**, *36*, 55–65. [CrossRef]
39. Simard, S.; Odziemkowski, M.; Irish, D.E.; Brossard, L.; Ménard, H. In situ micro-Raman spectroscopy to investigate pitting corrosion product of 1024 mild steel in phosphate and bicarbonate solutions containing chloride and sulfate ions. *J. Appl. Electrochem.* **2001**, *31*, 913–920. [CrossRef]
40. Alcántara, J.; Chico, B.; Simancas, J.; Díaz, I.; de la Fuente, D.; Morcillo, M. An attempt to classify the morphologies presented by different rust phases formed during the exposure of carbon steel to marine atmospheres. *Mater. Charact.* **2016**, *118*, 65–78. [CrossRef]
41. Dhaiveegan, P.; Elangovan, N.; Nishimura, T.; Rajendran, N. Weathering Steel in Industrial-Marine-Urban Environment: Field Study. *Mater. Trans.* **2016**, *57*, 148–155. [CrossRef]
42. Tamilselvi, M.; Kamaraj, P.; Arthanareeswari, M.; Devikala, S.; Selvi, J.A. Development of nano SiO2 incorporated nano zinc phosphate coatings on mild steel. *Appl. Surf. Sci.* **2015**, *332*, 12–21. [CrossRef]
43. Feng, Y.; Chen, S.; Zhang, H.; Li, P.; Wu, L.; Guo, W. Characterization of iron surface modified by 2-mercaptobenzothiazole self-assembled monolayers. *Appl. Surf. Sci.* **2006**, *253*, 2812–2819. [CrossRef]
44. Sandhyarani, N.; Skanth, G.; Berchmans, S.; Yegnaraman, V.V.; Pradeep, T. A Combined Surface-Enhanced Raman-X-Ray Photoelectron Spectroscopic Study of 2-mercaptobenzothiazole Monolayers on Polycrystalline Au and Ag Films. *J. Colloid Interface Sci.* **1999**, *209*, 154–161. [CrossRef]
45. Neff, D.; Bellot-Gurlet, L.; Dillmann, P.; Reguer, S.; Legrand, L. Raman imaging of ancient rust scales on archaeological iron artefacts for long-term atmospheric corrosion mechanisms study. *J. Raman Spectrosc.* **2006**, *37*, 1228–1237. [CrossRef]
46. Ohtsuka, T.; Tanaka, S. Monitoring the development of rust layers on weathering steel using in situ Raman spectroscopy under wet-and-dry cyclic conditions. *J. Solid State Electrochem.* **2015**, *19*, 3559–3566. [CrossRef]
47. Thierry, D. In-Situ Raman Spectroscopy Combined with X-Ray Photoelectron Spectroscopy and Nuclear Microanalysis for Studies of Anodic Corrosion Film Formation on Fe-Cr Single Crystals. *J. Electrochem. Soc.* **1988**, *135*, 305. [CrossRef]
48. Ohtsuka, T. Raman Spectra of Passive Films of Iron in Neutral Borate Solution. *Mater. Trans. Jim* **1996**, *37*, 67–69. [CrossRef]
49. Dubois, F.; Mendibide, C.; Pagnier, T.; Perrard, F.; Duret, C. Raman mapping of corrosion products formed onto spring steels during salt spray experiments. A correlation between the scale composition and the corrosion resistance. *Corros. Sci.* **2008**, *50*, 3401–3409. [CrossRef]
50. Demoulin, A.; Trigance, C.; Neff, D.; Foy, E.; Dillmann, P.; L'Hostis, V. The evolution of the corrosion of iron in hydraulic binders analysed from 46- and 260-year-old buildings. *Corros. Sci.* **2010**, *52*, 3168–3179. [CrossRef]
51. De la Fuente, D.; Alcántara, J.; Chico, B.; Díaz, I.; Jiménez, J.A.; Morcillo, M. Characterisation of rust surfaces formed on mild steel exposed to marine atmospheres using XRD and SEM/Micro-Raman techniques. *Corros. Sci.* **2016**, *110*, 253–264. [CrossRef]

52. Camí, G.E.; Chufán, E.E.; Pedregosa, J.C.; Varetti, E.L. Infrared and Raman spectra of 5-amino-1,3,4-thiadiazole-2-sulfonamide (Hats). Experimental data and quantum chemistry calculations. *J. Mol. Struct.* **2001**, *570*, 119–127. [CrossRef]
53. Weber, I.; Böttger, U.; Pavlov, S.G.; Hübers, H.W.; Hiesinger, H.; Jessberger, E.K. Laser alteration on iron sulfides under various environmental conditions. *J. Raman Spectrosc.* **2017**, *48*, 1509–1517. [CrossRef]
54. Chufán, E.E.; Pedregosa, J.C.; Borrás, J. Spectroscopic behaviour of metal–drug complexes. Infrared spectra of Cu(II) complexes with 5-amino-1,3,4-thiadiazole-2-thiol (Hatm). *Vib. Spectrosc.* **1997**, *15*, 191–199. [CrossRef]
55. Sherif, E.-S.M.; Erasmus, R.M.; Comins, J.D. In situ Raman spectroscopy and electrochemical techniques for studying corrosion and corrosion inhibition of iron in sodium chloride solutions. *Electrochim. Acta* **2010**, *55*, 3657–3663. [CrossRef]
56. Shen, S.; Zuo, Y.; Zhao, X. The effects of 8-hydroxyquinoline on corrosion performance of a Mg-rich coating on AZ91D magnesium alloy. *Corros. Sci.* **2013**, *76*, 275–283. [CrossRef]
57. Khan, G.; Basirun, W.J.; Kazi, S.N.; Ahmed, P.; Magaji, L.; Ahmed, S.M.; Khan, G.M.; Rehman, M.A.; Badry, A. Electrochemical investigation on the corrosion inhibition of mild steel by Quinazoline Schiff base compounds in hydrochloric acid solution. *J. Colloid Interface Sci.* **2017**, *502*, 134–145. [CrossRef]
58. Kaesche, H. (Ed.) Rusting of Iron and Steel. In *Corrosion of Metals: Physicochemicl Principles and Current Problems*, 1st ed.; Springer-Verlag: Berlin/Heidelberg, Germany, 2003; pp. 193–203. [CrossRef]
59. Génin, J.M.R.; Refait, P.; Olowe, A.A.; Abdelmoula, M.; Fall, I.; Drissi, S.H. Identification of Green Rust Compounds in the Aqueous Corrosion Processes of Steels; the Case of Microbially Induced Corrosion and Use of 78 K CEMS. *Hyperfine Interact.* **1998**, *112*, 47–51. [CrossRef]
60. Jafari, H.; Akbarzade, K.; Danaee, I. Corrosion inhibition of carbon steel immersed in a 1 M HCl solution using benzothiazole derivatives. *Arab. J. Chem.* **2019**, *12*, 1387–1394. [CrossRef]
61. Mahdavian, M.; Ashhari, S. Corrosion inhibition performance of 2-mercaptobenzimidazole and 2-mercaptobenzoxazole compounds for protection of mild steel in hydrochloric acid solution. *Electrochim. Acta* **2010**, *55*, 1720–1724. [CrossRef]
62. Amar, H.; Tounsi, A.; Makayssi, A.; Derja, A.; Benzakour, J.; Outzourhit, A. Corrosion inhibition of Armco iron by 2-mercaptobenzimidazole in sodium chloride 3% media. *Corros. Sci.* **2007**, *49*, 2936–2945. [CrossRef]
63. Gece, G.; Bilgiç, S. Quantum chemical study of some cyclic nitrogen compounds as corrosion inhibitors of steel in NaCl media. *Corros. Sci.* **2009**, *51*, 1876–1878. [CrossRef]
64. Ortega-Luoni, P.; Vera, L.; Astudillo, C.; Guzmán, M.; Ortega-López, P. Synthesis of Metallic Azoderivatives of 2-Amino-5-Mercapto-1,3,4-Thiadiazole. *J. Chil. Chem. Soc.* **2007**, *52*, 1120–1122. [CrossRef]
65. Guzmán, M.; Lara, R.; Vera, L. 5-Amino-1,3,4-Thiadiazole-2-Thiol Corrosion Current Density and Adsorption Thermodynamics on Astm A-890-1b Stainless Steel in A 3.5% NaC1 Solution. *J. Chil. Chem. Soc.* **2009**, *54*. [CrossRef]